NANOSCALE $Cu_{0.5}Zn_{0.5}Fe_2O_4$ FERRITES HOSTED IN MESOPOROUS TiO_2-MO_2 (M=Ce, Zr, Sn) MIXED OXIDES FOR SUSTAINABLE ENVIRONMENTAL PROTECTION

Tanya Tsoncheva

Institute of Organic Chemistry with Centre of Phytochemistry, Bulgarian Academy of Sciences, Ak. G. Bonchev str. Bl.9, 1113 Sofia, Bulgaria

Abstract

This study is aimed at the preparation of homogeneous, nanostructured and high surface area titania doped with CeO_2, ZrO_2 and SnO_2 mesoporous oxides. These materials are used as a host matrix of $Cu_{0.5}Zn_{0.5}Fe_2O_4$ ferrite nanoparticles. The obtained composites are characterized by a complex of physicochemical techniques, such as nitrogen physisorption, XRD, SEM, HRTEM, Temperature – programmed reduction with hydrogen, XPS, UV-Vis and Moessbauer spectroscopies. Their catalytic behavior is tested in methanol decomposition as a source of hydrogen and total oxidation of ethyl acetate as a representative volatile organic compound. A synergistic activity between the acidic sites on the mixed oxide surface and the redox transitions in the hosted on them ferrite nanoparticles is well established. This effect is in a complex dependence on the surface and texture characteristics of the mesoporous TiO_2-MO_2 host matrix. The catalytic properties in both catalytic processes are optimized using mesoporous TiO_2-CeO_2 mixed oxide as a support of the $Cu_{0.5}Zn_{0.5}Fe_2O_4$ ferrite nanoparticles.

Keywords: *mesoporous oxides, TiO_2-CeO_2, TiO_2-ZrO_2, TiO_2-SnO_2, $Cu_{0.5}Zn_{0.5}Fe_2O_4$ ferrite modifications, methanol decomposition, ethyl acetate oxidation*

1. INTRODUCTION

The accelerated urbanization and industrialization and the related problems with the environmental pollution and depletion of the fossil fuels are of permanently increasing world-wide interest. In response, in December 2020 more than 190 Parties of the Paris Agreement ratified the need of the greenhouse emissions reduction by at least 55% by 2030 from 1990 levels *via* adequate economic and social transformations based on the best available science [1].

Nowadays, the transport is assumed responsible for over 25% of the emissions. More and more countries established the carbon neutrality targets in this sector and hydrogen, which could be produced from available sources, such as water or biomass, is considered as the most effective alternative to the non-renewable fuels, with carbon-zero emissions [2]. According to the International Energy Agency model, more than double demand of hydrogen between 2020 and 2030 and up to 6-fold increase in 2050 are predicted to meet the net zero targets. Nowadays the main challenges in the hydrogen economy are related to the safety storage and supply the industrial and mobile installations with hydrogen *via* minimum investments for the changes of the existing infrastructure [3,4]. The liquid organic compounds could be a good solution in this aspect, especially for the applications in transport and miniature devices. Methanol gains a considerable attention due to its high H/C molar ratio, production in significant amount by well- known technologies from diverse sources, also from renewable ones, and possibility to release hydrogen under relatively mild conditions [5-7]. Methanol decomposition is a promising, simple and economically feasible way for hydrogen release without using any additional reactants, such as water (steam reforming), oxygen (partial oxidation) or CO_2 (dry reforming) and also, recovering the heating costs by burning of the CO by-product [6].

The Convention on Long-range Transboundary Air Pollution [8] determines the Volatile organic compounds (VOCs) as the dominant air pollutants due to their toxic, volatile and carcinogenic features, leading also to serious climate changes *via* formation of ground-level ozone, aerosol and smog. They are emitted from large scale of sources, such as solvents, petroleum, agriculture, organic chemical, food and steel industries and represents a subject of strict regulation and control. Adsorption, condensation, membrane separation, biological degradation, non-thermal plasma oxidation, photocatalytic

decomposition, thermal incineration etc. are the main methods which have been explored for the VOCs elimination. The catalytic total oxidation of VOCs is a preferable low-energy consuming and, due to the low level of harmful by-products, environmentally friendly technology [9-11].

The optimization of the catalysts design is the most important approach for the achievement of maximum benefits during the catalytic processes. Generally, the transition metal-based catalysts reveal unlimited potential in this aspect due to their low price and possibility to be combined in composites with improved texture, tunable structure and morphology and variable surface and redox characteristics [6, 9-11]. Nowadays the magnetic ferrites with spinel structure have been considered as promising catalysts alternative due to their unique properties, low cost, abundance and possibility for easily recovering after the catalytic process by the magnetic separation [12-16]. The ferrites can be described as a cubic close-packed arrangement of oxygen ions, where the M^{2+} and Fe^{3+} ions occupy tetrahedral (A) and octahedral (B) positions. The cation distribution in this structure can be described as $(M_xFe_{1-x})^A[M_{1-x}Fe_{1+x}]^BO_4$, where *x* is the inverse parameter with values 0 or 1 for the inverse and the normal spinel, respectively and with intermediate values, for the partially (mixed) inverse spinels. The higher exposure of the metal ions in the octahedral sublattice to the reactants provides their key role during the catalytic process [17]. Obviously, the nature and the distribution of the metal ions in the spinel lattice are responsible for their magnetic, optic and catalytic properties, which could be also affected by the miniaturization of the ferrite particles. Most of the bulk copper ferrites ($CuFe_2O_4$) is determined as inverse spinels and zinc ferrite ($ZnFe_2O_4$) is typical example of normal ferrite. Depending on the composition, the $Cu_xZn_{1-x}Fe_2O_4$ mixed ferrites represent diverse distribution of cations between the A and B sites, with a preferable location of Cu^{2+} ions in the octahedral positions and Zn^{2+} ions on the tetrahedral ones.

The ferrite deposition on different supports could change their behaviour *via* either particles size control or generation of electron transfer effects from the support to the spinel particles and vice versa. These effects could be more complicated for the porous supports, where the pores not only restrict the growth of the ferrite particles, but also, regulate their availability to the reactants. Titania is an active reducible catalyst support, generally providing strong interaction with the active phase and more importantly, it is a low-cost, widely available and environmentally friendly material [6,18]. The problems, related to its low surface area and sintering at high temperature, could be overcome by doping with different metal oxides. Mixed TiO_2-ZrO_2 oxides provide improvement of the surface area and mechanical strength of the individual titanium and zirconium oxides with a simultaneous fine tuning of their acid-base and redox properties [19-22]. Doping titania with the isostructural and aliovalent oxides, like SnO_2, accelerates the anatase to rutile phase transformations, formation of substituted composites, reduction of crystal size, increase of surface acidity and decrease in the band-gap energy [23,24]. Many authors assumed that the addition of CeO_2 to TiO_2 decreases the particle size, increases the surface area and thermal stability, stabilizes the anatase phase, reduces the band-gap energy and improves the oxygen storage capacity [25].

The template assisted hydrothermal technique allows the synthesis of mixed metal oxides under relatively mild conditions, producing materials in a narrow particle size distribution and controlled morphology, well developed porous texture and tunable surface characteristics. In our previous study a successful synthesis of mesoporous TiO_2-CeO_2 [26]; TiO_2-ZrO_2 [27] and TiO_2-SnO_2 [28] mixed oxides with diverse composition by using of hydrothermal synthesis in presence of N-hexadecyl-N,N,N-trimethylammoniumbromide (CTAB) as structure directing agent, was reported. This investigation is focused on the application of the TiO_2-MO_2 (M=Ce, Zr, Sn) mixed oxides with equimolar M/Ti ratio as a host matrix of $Cu_{0.5}Zn_{0.5}Fe_2O_4$ ferrite nanoparticles. The obtained composites were characterized in details by Nitrogen physisorption, XRD, HRTEM, UV-Vis, XPS, Moessbauer spectroscopy and TPR with hydrogen. Methanol decomposition as a source of hydrogen and total oxidation of ethyl acetate with a potential for VOCs elimination in air were applied as catalytic tests.

2. MATERIALS AND METHODS

2.1. Materials

The TiO_2-MO_2 mixed oxides were synthesized using template-assisted hydrothermal technique. Typically, 12.0 g CTAB were dissolved in 100 ml distilled water and mixed with a second solution of $TiCl_4$ and MCl_4 (M=Ce, Zr, Sn) (Ti/M mol ratio of 1) in 50 ml distilled water. Then, the temperature was raised to 323 K and the reaction mixture was stirred for 30 min before adding of 20 ml NH_4OH (25%). The resulting mixture was stirred overnight at 323 K, then transferred into autoclave and treated at 373 K for 24 h. The obtained samples were filtrated, washed with distilled water, dried at room temperature and calcined up to 773 K with a ramp of 1 °K/min and dwelling time of 10 h at the end temperature. Thus obtained mixed oxides were denoted as TiCe, TiZr and TiSn, respectively.

The obtained materials were impregnated with an aqueous solution of $Cu(NO_3)_2.6H_2O$; $Zn(NO_3)_2.6H_2O$ and $Fe(NO_3)_3.9H_2O$ (Cu:Zn:Fe mol ratio of 0.5:0.5:2). After drying at room temperature, the samples were calcined in air at 770 K for 2 h. The obtained modifications were denoted as FrTiM, where M=Ce, Zr or Sn.

Similar supported on silica (BET=300m^2g^{-1}) ferrite modification (FrSi) was also obtained.

2.2. Methods and apparatus

The texture characteristics of the obtained materials were studied by nitrogen adsorption- at 77 K on a Beckman Coulter SA 3100 apparatus. Brunauer-Emmett-Teller (BET) surface was calculated using the data for the adsorbed nitrogen within 0.08 and 0.3 relative pressures; total pore volume was acquired by the amount of adsorbed nitrogen at about 0.99 relative pressure and the pore size distribution was obtained by Barrett–Joyner–Halenda (BJH) method using the desorption branch of the isotherms.

Powder X-ray diffraction study was performed on a Bruker D8 Advance diffractometer with Cu Kα radiation (λ=1.5406 Å) and a LynxEye detector with constant step of 0.02° 2θ and counting time of 17.5 s per step. Mean crystallite size were determined by the Topas-4.2 software.

The UV–Vis spectra were collected on a Jasco V-650 UV-Vis spectrophotometer.

The surface composition of the samples and the chemical states of the elements were inspected by X-ray photoelectron spectroscopy (XPS) using a SPECS PHOIBOS 100 hemispherical analyzer with a 5-channel detector and a SPECS XR50 X-ray source equipped with an Al and Mg dual anode. The measurements were performed with Al anode at Epass 40eV for survey spectra and Epass 10eV for high resolution spectra. The acquired data were processed in CasaXPS software with Shirley background profile and built in RSF were used for calculation of the compositions from high resolution spectra.

The morphology of the samples was measured on a FEI Talos F200X transmission electron microscope. The pyridine desorption spectra were collected with a BioRad FTS-60 spectrophotometer using sample disks and preliminary dehydration under vacuum at 383 K for 1 h.

The amount of adsorbed pyridine was calculated on the basis of the relationship reported by Emeis et al. [29] from the spectra registered at 423 K and integration of the band at around 1455 cm^{-1} and 1545 cm^{-1} for Lewis and Bronsted acidity, respectively.

The Mössbauer spectra were recorded on a Wissel (Wissenschaftliche Elektronik GmbH, Germany) electromechanical spectrometer at room temperature or under the temperature of liquid nitrogen (LNT). A ^{57}Co/Rh (activity ≈ 10 mCi) source and α-Fe standard as well as a WinNormos software for the picks fitting were used. The TPR/TG (temperature-programmed reduction/ thermo-gravimetric) analyses were performed on a Setaram TG92 instrument in 100 cm^3 min^{-1} flow of H_2 in Ar (volume ratio of 1) and heating rate of 5 K min^{-1}.

2.3. Catalytic tests

2.3.1. Total oxidation of ethyl acetate

The total oxidation of ethyl acetate was carried out in a flow type reactor using 0.030 g of catalyst and a mixture of ethyl acetate in air (1.21 mol%). WHSV was 100 h^{-1}. Before the catalytic experiments the

samples were treated in argon at 373 K for 1 h and after testing the initial flow composition, the catalytic data were obtained under temperature programmed regime in the range of 473–773 K. Gas chromatographic analyses were performed on a HP 5890 apparatus using carbon-based calibration. The products selectivity was calculated as S_{CO2} for CO_2, S_{AA} for acetaldehyde, S_{Et} for ethanol, $S_{C2H4}$for ethene and S_{AcAc} for acetic acid by the equation: $S_i = Y_i/X*100$, where S_i and Y_i were the selectivity and the yield of (i) product and X was the conversion (50%). The specific catalytic activity (SA) was calculated as SA = X/A, where X was the conversion at 650 K and A was the specific surface area.

2.3.2. Methanol decomposition

Methanol conversion was performed in a fixed bed flow reactor with 0.055 g of catalyst, argon as a carrier gas (50 cm^3min^{-1}) and methanol partial pressure of 1.57 kPa. The catalysts were tested under temperature-programmed regime within the range of 350–770 K with heating rate of 1 K min^{-1}. On-line gas chromatographic analyses were performed on HP apparatus equipped with a flame ionization detector and a detector of thermo-conductivity on a PLOT Q column, using an absolute calibration method and a carbon based material balance. The selectivity (S) to CO, CO_2, CH_4 and dimethyl ether (DME) was calculated as $S_i = Y_i/X*100$, where Y_i was the yield of (i) product and X was the conversion (30%). The specific catalytic activity (SA) was calculated as SA = X/A, where X was the conversion at 700 K and A was the specific surface area.

3. RESULTS AND DISCUSSION

3.1. Structural characterization

The texture of the obtained materials was studied by low-temperature physisorption of nitrogen. The adsorption-desorption isotherms and pore size distribution for the parent TiO_2-MO_2 mixed oxide supports are presented in Figure 1. Data for the BET surface area and total pore volume for the TiO_2-MO_2 mixed oxide supports and their ferrite modifications are listed in Table 1.

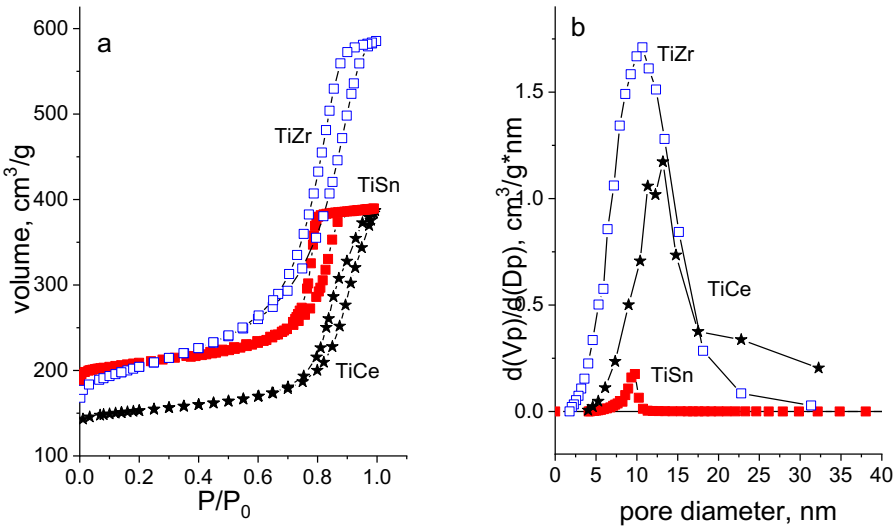


Fig. 1. Nitrogen physisorption isotherms (a) and pore size distribution (b) of TiO_2-MO_2 supports

The physisorption isotherms of the TiO_2-MO_2 supports represented a significant jump above 0.7 relative pressure due to the condensation of nitrogen in the pores. The isotherms are of type IV according to the IUPAC classification, which is typical of mesoporous materials. The shape of the hysteresis loop is of type H1 in case of TiO_2-ZrO_2, evidencing presence of almost cylindrical mesopores with average size of 12 nm. The hysteresis loop for TiO_2-CeO_2 is of type H3, indicating presence of interparticle pores with wider size distribution. The observed H2 hysteresis loop for the TiO_2-SnO_2 support is typical of

"ink-bottle" type pores. For this sample, presence of smaller mesopores, which ensure significantly low pore volume, was detected. In comparison with the other supports, TiO_2-ZrO_2 possesses about 2.5 times higher BET surface area and 1.7-2 times larger pore volume.

After the modification with $Cu_{0.5}Zn_{0.5}Fe_2O_4$, a decrease in the BET surface area and pore volume of the TiO_2-MO_2 mixed oxides was observed (Table 1), which could be assign to the deposition of ferrite nanoparticles within the pores of the support. These changes were significant for FrTiSn, most probably due to the blocking of the small pore entrances, typical of the TiO_2-SnO_2 support (Fig. 1).

XRD patterns of the ferrite containing composites are shown in Fig. 2 and data for the phase composition and average crystallite size are summarized in Table 1. The XRD pattern of FrTiSn represented reflections at around 26.5°, 34.1°, 54.3° and 64.9° 2Θ, which correspond to (110), (101), (220) and (301) crystallographic planes of tetragonal cassiterite phase (PDF 41-1445) with average crystallite size of 5 nm.

Table 1. Specific surface area (S_{BET}) , total pore volume (V_{tot}), phase composition and average crystallite size of TiO_2-MO_2 supports and their $Cu_{0.5}Zn_{0.5}Fe_2O_4$ ferrite modifications.

Sample	S_{BET}, m^2g^{-1}	V_{tot}, cm^3g^{-1}	Phase composition	Crystallite size, nm
TiCe	99	0.45	cerianite	12
FrTiCe	90	0.37	cerianite	13
TiZr	256	0.69	amorphous	
FrTiZr	198	0.56	amorphous	
TiSn	107	0.32	cassiterite	5
FrTiSn	69	0.17	cassiterite	5

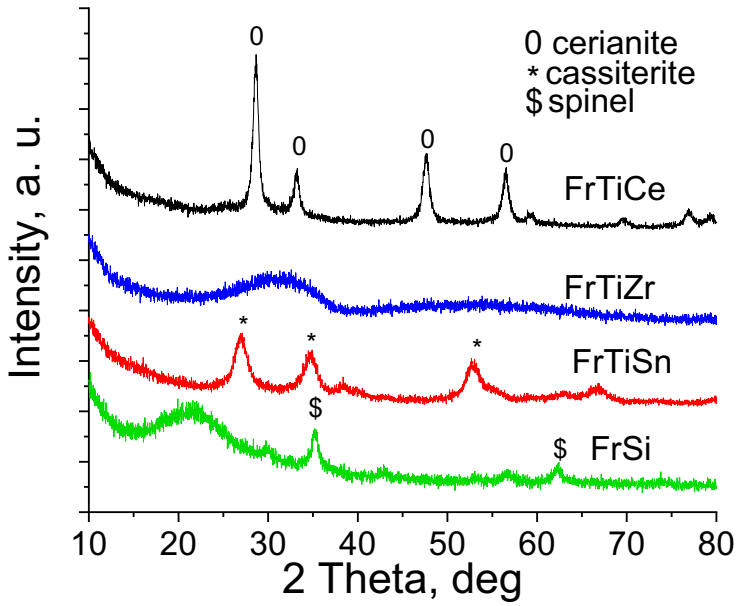


Fig. 2. XRD patterns of $Cu_{0.5}Zn_{0.5}Fe_2O_4$ ferrite modified TiO_2-MO_2 (M=Ce, Zr, Sn) mixed oxides. For comparison, the corresponding silica modification is presented.

The diffraction features at 2 Θ 28.6º, 33.3º, 47.8º and 56.4 º in the pattern of FrTiCe indicated (111), (200), (220) and (311) planes of cubic fluorite structure of cerianite (PDF 00-0065-5923). The average crystallite size was about 12-13 nm. The reflections in the FrTiZr pattern were very broad, which indicates very high dispersion of the metal oxide components and this well correlates with the highest BET surface area of this sample (Table 1).

In case of all TiO_2-MO_2 ferrite modifications, no additional reflections, typical of ferrite phase could be distinguished. In contrast, the observed features at 35.7º, 43.2º, 56.1º and 62.4º 2 Θ in the pattern of the reference FrSi correspond to (311), (400), (511) and (440) planes of cubic spinel phase. Thus, the mesoporous TiO_2-MO_2 supports promote the formation of very finely dispersed ferrite phase.

This assumption was well illustrated by the HRTEM-EDS images of the samples (Fig. 3). The homogeneous penetration of titania and MO_2 oxides in the supports was well-illustrated in the figures from the left side of Fig. 2.

The regular distribution of Cu, Zn and Fe-containing species, which seems to be also in close contact between themselves, could be attributed to the formation of ferrite phase, homogeneously dispersed all over the whole support.

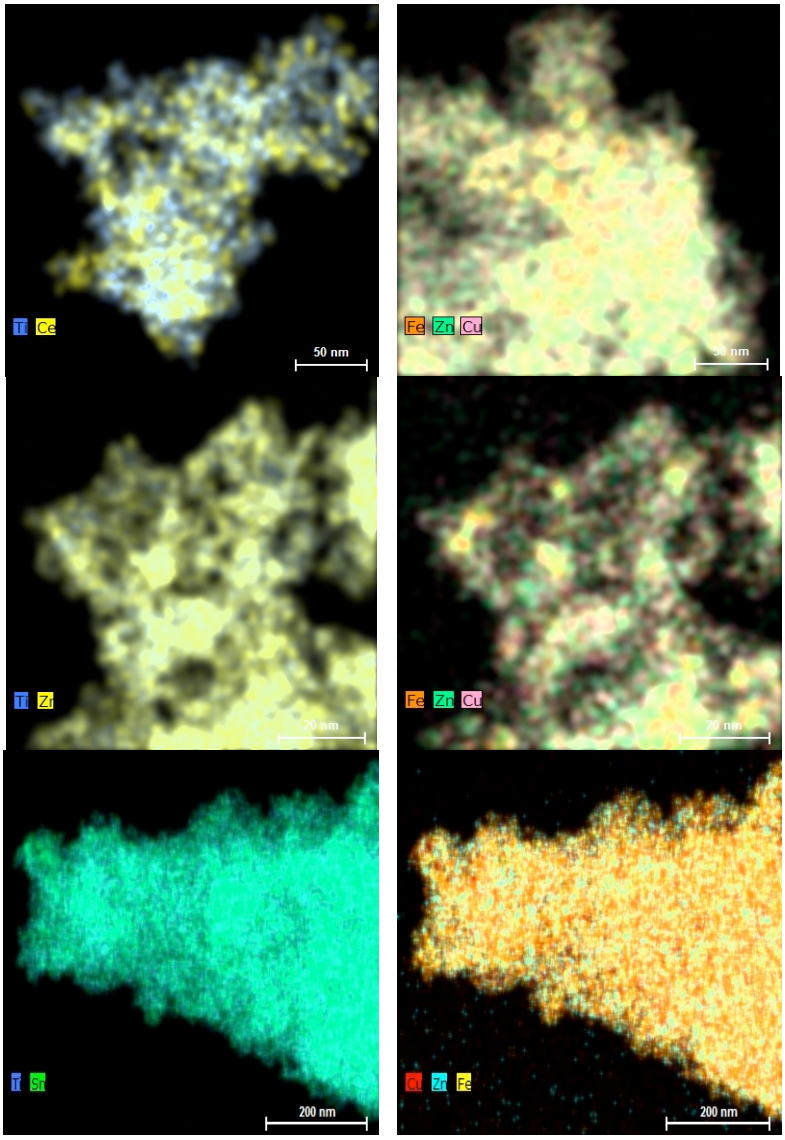


Fig. 3. HRTEM-EDS images of (from top to bottom) TiO_2-CeO_2, TiO_2-ZrO_2 and TiO_2-SnO_2 (left) and the corresponding ferrite modifications (right).

3.2. Spectroscopic study

In Fig. 4 are shown the UV-Vis spectra of the ferrite supported composites. The dash lines illustrate the absorption of the corresponding TiO_2-MO_2 supports. For more precise interpretation, the UV-Vis spectrum of FrSi is also shown. The broad absorption feature at 310-360 nm in the spectrum of TiSn could be assigned to the ligand to metal electron transfer in highly defective cassiterite-like structure [30-32]. The absorption age in the spectrum of TiCe is red shifted as reported for the pure titania (around 355 nm) and ceria (314 nm) [25], which evidences formation of solid solution. Similar effect was detected for the TiZr support [33].

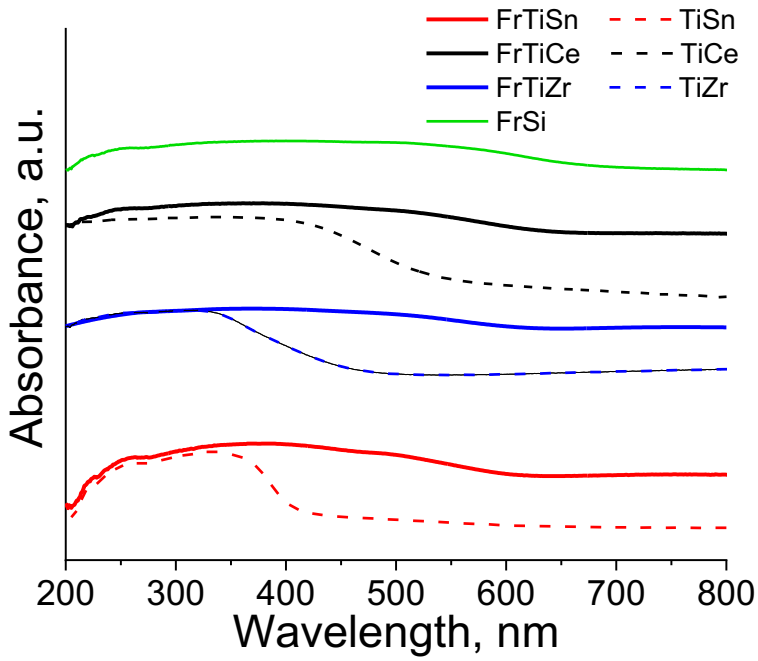


Fig. 4. UV-Vis spectra of various $Cu_{0.5}Zn_{0.5}Fe_2O_4$ ferrite modified TiO_2-MO_2 (M=Ce, Zr, Sn) mixed oxides. For comparison: TiO_2-MO_2 supports and $Cu_{0.5}Zn_{0.5}Fe_2O_4$ modified silica are presented.

The modification of TiO_2-MO_2 with $Cu_{0.5}Zn_{0.5}Fe_2O_4$ resulted in a strong absorption feature in the 420-650 nm region, which could be attributed to the ligand to metal electron transfer in the ferrite phase. The slight blue-shift of these peaks as compared to the UV-Vis spectrum of the reference FrSi sample, suggests strong interaction between the loaded ferrite particles and TiO_2-MO_2 supports.

In order to obtain knowledge for the surface composition of the samples, XPS spectra of the TiO_2-MO_2 mixed oxide supports were recorded. The Ti 2p spectra consisted of two peaks at ca. 458.5 and 464.2 eV, attributable to Ti $2p_{3/2}$ and Ti $2p_{1/2}$ spin-orbit peaks. The Ti $2p_{3/2}$ peak was successfully fitted with two components with binding energies (BE) of 458.5 and 455.9 eV for TiO_2 and Ti_2O_3, respectively [34].

The Ce 3d core level spectra are fitted with ten peaks attributable to Ce $3d_{5/2}$ and Ce $3d_{3/2}$ spin-orbit splitting in CeO_2 and Ce_2O_3[35].

The peaks with BE of about 331.9-332.1 eV in the Zr 3p spectra correspond to Zr $3p_{3/2}$ in ZrO_2 phase [36].

The Sn 3d spectra exhibited doublet peaks at ca. 486.1 and 494.5 eV, corresponding to Sn $3d_{5/2}$ and Sn $3d_{3/2}$ spin-orbit splitting. The Sn $3d_{5/2}$ peaks were well-fitted with three components with BE of 486.6, 485.9 and 485.0 eV, which could be assigned to Sn^{4+} and Sn^{2+} in different environment [37].

The surface distribution of various metal ions in the MO_2 oxides and the corresponding suboxides, as well as the O content are presented in Table 2.

Table 2. Surface composition of TiO_2-MO_2 supports, determined by the XPS analyses.

Sample	M^{4+}	$M^{4+-\delta}$	Ti^{4+}	Ti^{3+}	O	M/Ti
TiCe	8.67	4.29	15.06	2.74	69.24	0.72
TiZr	16.85		4.35	8.11	70.69	1.35
TiSn	20.21	2.15	11.61	1.29	60.30	1.73

The M/Ti ratio differed from the expected for the equimolar solid solution and increased in the order TiCe>TiZr>TiSn. This non-homogeneous metal ions distribution could be assigned to different rate of metal hydroxides precipitation, which results in a "core/shell" model of the mixed oxides formation. Thus, predominant presence of Zr and Sn oxides in the "shell" of the TiZr and TiSn solids, respectively, could be assumed, while the ceria occupy mainly the "core" positions in the TiCe system. For the latter, the observed significant amount of Ce^{3+} defects could be attributed to the formation of highly distorted Ti-O-Ce interface layer. In case of TiZr, its formation is evidenced by the existence of high amount of Ti^{3+} defects, while formation of Sn^{2+} and Ti^{3+} ions co-exist as a result of the insertion of Ti^{4+} in SnO_2 or vice versa.

In Table 3 are shown data from the pyridine adsorption for the TiO_2-MO_2 supports.

Table 3. Pyridine adsorption on various TiO_2-MO_2 supports.

Sample	mmolPy/g	mmolPy/m^2*10^{-3}
TiCe	0.08	0.79
TiZr	0.30	1.20
TiSn	0.05	0.47

Presence of big number, predominantly Lewis acidic sites, was established for the TiZr composite, followed by TiCe and TiSn. The order of the acidity changes was preserved after the normalization of the adsorbed pyridine to unit specific surface area, which indicates different distribution of the acidic sites with respect to their strength and density.

Moessbauer spectra were recorded in order to obtain more information for the Fe-containing phases in the TiO_2-MO_2 modifications. In Table 4 are summarized data for the isomer shift (IS), quadruple splitting (QS), hyperfine magnetic field (H_{eff}), line width (FWHM) and relative weight of each component (G) for various ferrite modifications.

Table 4. Moessbauer parameters of various initial modifications and selected ones, after the methanol decomposition catalytic test (cat).

Sample	Components	IS, mm/s	QS, mm/s	H_{eff}, T	FWHM, mm/s	G, %
FrTiCe	Db 1 -Fe^{3+}_{octa}	0.35	0.70	-	0.38	49
	Db 2 -Fe^{3+}_{octa}	0.33	1.15		0.48	51
FrTiCe_cat	Db 1 -Fe^{3+}_{octa}	0.35	0.76	-	0.40	43
	Db 2 -Fe^{3+}_{octa}	0.34	1.22		0.52	57

FrTiZr	Db 1 -Fe^{3+}_{octa}	0.34	0.74	-	0.40	46
	Db 2 -Fe^{3+}_{octa}	0.33	1.26		0.49	54
FrTiZr _cat	Db 1 -Fe^{3+}_{octa}	0.34	0.83	-	0.41	41
	Db 2 -Fe^{3+}_{octa}	0.34	1.35		0.51	59
FrTiSn	Db1-Fe^{3+}_{octa}	0.36	0.68	-	0.36	44
	Db2-Fe^{3+}_{octa}	0.33	1.21		0.54	56
FrSi	Db 1 -Fe^{3+}_{octa}	0.34	0.48	-	0.39	54
	Db 2 -Fe^{3+}_{octa}	0.33	0.89		0.60	46
FrSi _cat	Sx- Fe_3C	0.20	0.02	19.1	0.73	27
	Db 1 -Fe^{3+}_{octa}	0.36	0.63	-	0.42	29
	Db 2 -Fe^{3+}_{octa}	0.36	1.08	-	0.55	44

The Moessbauer spectra of all materials were well fitted with two doublets with isomer shift (IS) of 0.33-0.35 mm/s and relatively high QS. They probably originate with the Fe^{3+} ions, distributed in the "core" and "shell" of very finely dispersed (10-12 nm) ferrite particles with superparamagnetic behavior. No significant effect of the nature of the support on the state of the loaded ferrite phase could be assumed. However, the slightly higher "core/shell" ratio for the reference FrSi sample reveals lower dispersion of the ferrite particles on the silica support. This assumption is in line with the data obtained by the XRD and UV-Vis analyses.

3.3. TPR characterization

In Fig. 5 are demonstrated data from the TPR-TG analyses of various ferrite modifications. The TPR profile of the reference FrSi sample consisted of two well-defined effects, centered at 420 and 582 K due to the decomposition of $Cu_{0.5}Zn_{0.5}Fe_2O_4$ to Cu, ZnO and magnetite. The continuous weight loss above 700 K is probably related to further reduction transformations of the magnetite particles to metallic iron.

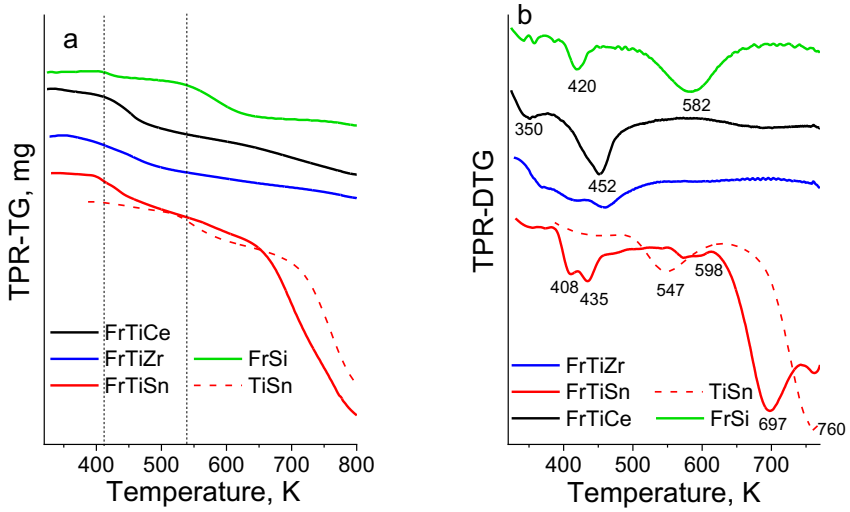


Fig. 5. TPR-TG (a) and TPR-DTG (b) profiles for various $Cu_{0.5}Zn_{0.5}Fe_2O_4$ ferrite modified TiO_2-MO_2 (M=Ce, Zr, Sn) mixed oxides. For comparison-data for the TiO_2-SnO_2 support and $Cu_{0.5}Zn_{0.5}Fe_2O_4$ modified silica are presented.

These features were also well-resolved in the TPR profile of FrTiCe, but they were significantly shifted to lower temperature as compared to FrSi. In line with the XRD (Fig. 2), Moessbauer (Table 4) and UV-Vis (Fig. 4) data, this could be attributed to higher dispersion of the ferrite particles on TiO_2-CeO_2, which is promoted both by the mesoporous texture of the support (Table 1) and the strong interaction of ferrite particles with the surface Lewis acidic sites (Table 3). Additional labilization of the oxygen ions in the ferrite particles by the influence of the strongly basic sites on the TiO_2-CeO_2 support is expected as well.

Several overlapping low-temperature TPR effects are detected for the TiO_2-ZrO_2 supported ferrite, indicating easier reduction transformations as compared to FrTiCe.

The TPR features are more significant for FrTiSn, due to the simultaneous 'spilover"-assisted reduction transitions with the TiSn support and loaded on it ferrite particles to metallic Cu, Sn and Fe.

3.4. Catalytic tests

3.4.1. Ethyl acetate oxidation

In Fig. 6a are presented the temperature dependencies of ethyl acetate (EA) oxidation. The catalyst supports possessed catalytic activity above 530-550 K for TiCe and TiZr and above 620 K for TiSn. For the former two samples about 100% conversion was achieved at 650-680 K, while for the latter, maximum 60 % conversion was registered at 750 K. The CO_2 selectivity varied between 50-70% (Fig. 6b). About 25% ethanol, 11-16% acetaldehyde (AA) and up to 9% acetic acid (AcAc) were detected for TiCe and TiZr, while mainly acetaldehyde (up to 25%) was found for TiSn. As reported before [26-28], the EA oxidation is a step-wise process, where initially EA hydrolysis to acetic acid and ethanol over the acidic sites occurs, and further, the intermediate products oxidize to CO_2 over the redox sites, following Mars van Krevelen mechanism. Obviously, managing the balance between the different catalytic sites, fine tuning of the catalyst activity and selectivity could be achieved. Thus, the highest acidity in the TiCe and TiZr (Table 3) probably promotes the hydrolysis of EA, while the second stage of ethanol and acetic acid oxidation to AA and CO_2 is facilitated by the dominant Sn^{2+}/Sn^{4+} redox pairs on the surface of TiSn (Table 2). In order to precise this assumption, the specific activity per unit surface area was also calculated (Fig. 6c). Here, the extremely high specific activity for TiCe could be related to the high surface density of acidic (Table 3) as well as Ce^{3+}/Ce^{4+} and Ti^{3+}/Ti^{4+} (Table 4) redox pairs. Just the opposite, despite the high density of the acidic sites in TiZr (Table 3), the presence of small number of highly diluted Ti^{3+}/Ti^{4+} redox pairs suppresses the total oxidation of the intermediates.

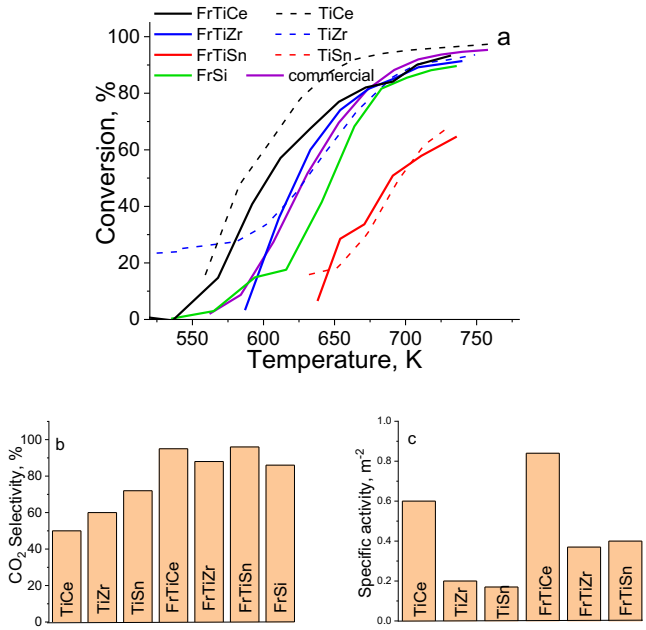


Fig. 6. Ethyl acetate oxidation vs temperature (a), CO_2 selectivity at 50% conversion (b) and specific activity at 650 K (c) for various composites.

The modification of the supports with ferrite provides increase in the specific catalytic activity (Fig. 6c) and decrease of the amount of the intermediates with a simultaneous increase in the CO_2 selectivity (Fig. 6b). On the base of the TPR measurements (Fig. 5), additional impact of the ferrite nanoparticles on the redox potential of the composites could be assumed. The main contribution of the Cu^{2+}/Cu^{+} redox pairs, situated on the more exposed to the reactants octahedral positions in the ferrite sub-lattice could be proposed.

Note that FrTiCe and FrTiZr composites possessed improved catalytic activity as compared to the commercial Pt-containing catalyst and also, to the supported on the silica ferrite. The latter effect could be related to the improved ferrite dispersion, facile electron exchange between the ferrite particles and support and synergistic effects between the acidic sites from the TiM support and the redox sites from the loaded ferrite particles.

3.4.2. Methanol decomposition

In Fig. 7 are shown data for methanol decomposition on various materials. The TiM supports possessed catalytic activity in methanol decomposition above 550-600 K for TiZr and TiCe, respectively, with the achievement of about 70-80% conversion at 650-700 K (Fig. 7a). For TiCe, besides CO (Fig. 7b), methane is observed as the main by-product, while significant amount of dimethyl ether (DME) was also formed on the TiZr support. In line with the acidity data (Table 3), interaction of methanol with surface acidic sites with the formation of methoxy groups and their further decomposition to CO could be assumed. The surface methoxy groups could also interact with the nearby adsorbed methanol molecule or with the neighbored methoxy and hydroxyl groups, leading to the formation of DME and methane, respectively. The specific activity of TiCe was slightly higher as compared to TiZr (Fig. 7c), which indicates that the observed much higher catalytic activity of the latter is predominantly related to its higher surface area (Table 1) and high density of acidic sites (Table 4) on it.

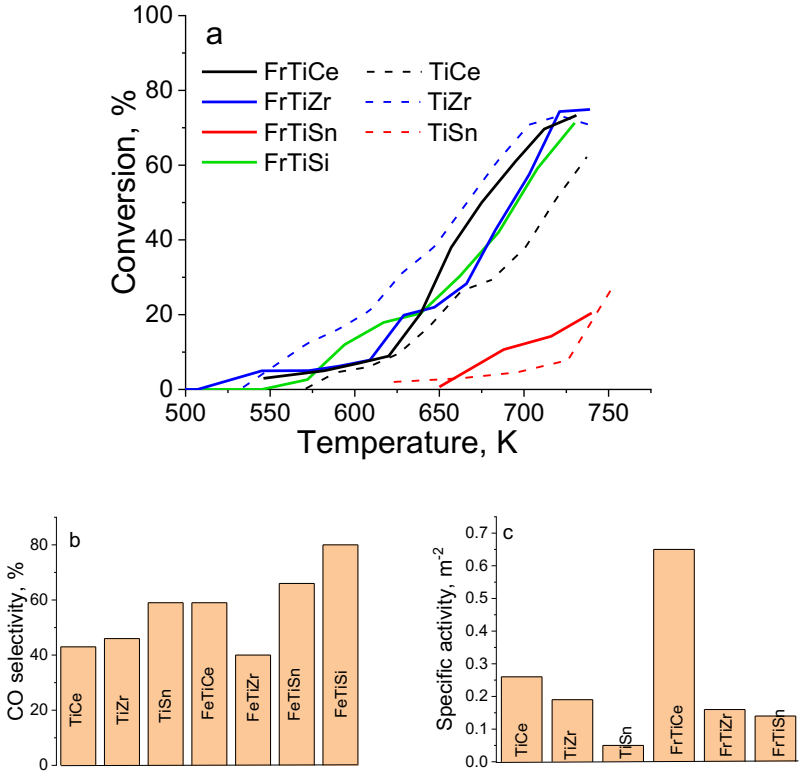


Fig. 7. Methanol decomposition vs temperature (a), CO selectivity at 30% conversion (b) and specific activity at 700 K(c) for various composites.

The TiSn support possessed catalytic activity above 700 K and up to 20% conversion was registered at 750 K. The selectivity to CO was higher as compared to the other supports and up to 30% methane was registered as by-product. In consistent with the acidic measurements (Table 3), this behavior is mainly related to the low density of acidic sites on the TiSn surface, which suppressed the formation of surface methoxy intermediates.

The modification of TiM oxides with ferrite influenced the catalytic behavior in different way. The decrease in the catalytic activity for FrTiZr is accompanied with preservation of the CO selectivity and specific catalytic activity. This reveals predominant activity of the surface acidic sites on TiZr, which number slightly decreased with the decrease of the BET surface area of FrTiZr. It seems that in this sample the finely dispersed ferrite particles are in a high extent blocked in the long mesopores of the TiZr support, being non-accessible for the reactant molecules.

Just the opposite was the case of FrTiCe. Here, a significant increase in the total catalytic activity (Fig. 7a) and specific activity (Fig. 7c), combined with a simultaneous increase in the CO selectivity (Fig. 7b) and decrease in the methane formation, were observed. Obviously, this is strongly related to the own activity of the finely dispersed ferrite phase on TiCe support. This supposition is confirmed by the significantly high catalytic activity (Fig. 7a) and CO selectivity (Fig. 7b), which were observed for the reference FrSi sample. The significantly higher selectivity to methane (up to 17%) and DME (about 7%) for FrTiCe clearly demonstrates the activity of the acidic sites from the support. A synergistic effect between them and the loaded ferrite particles could be assumed. The ferrite modification of TiSn slightly improved the specific catalytic activity and CO selectivity. In accordance with the reduction data (Fig. 5), this behaviour could be attributed to the reduction changes both with TiSn and ferrite particles to metals (alloys). The reduction changes with the ferrite phase in FrSi were well illustrated by the Moessbauer spectra of the used in the catalysis sample, where a significant amount of Fe_3C appeared (Table 4). For comparison, these transformations were not detected for the FrTiCe and FrTiZr catalysts, most probably due to the very fine dispersion of the active phase in them.

4. CONCLUSION

High quality homogeneous mesoporous composites of hosted in TiO_2-MO_2 (M=Ce, Zr, Sn) finely dispersed $Cu_{0.5}Zn_{0.5}Fe_2O_4$ ferrite nanoparticles were prepared by combination of the template assisted hydrothermal technique and incipient wetness impregnation procedure. The high density of acidic sites and Ce^{3+}/Ce^{4+} redox pairs in FrTiCe composite promotes the catalytic activity in total oxidation of ethyl acetate and methanol decomposition by facile electron exchange with the loaded ferrite nanoparticles and generation of sinergistic effects. The blocking of the ferrite nanoparticles in the long mesopores of the FrTiZr composite provides significantly lower density of redox sites and ensures predominant activity of surface acidic functionality, which slightly improves the catalytic behaviour of the TiZr support. The presence of SnO_2 in the composites significantly decreases the surface acidity and change the samples composition under the reduction conditions, which provides significantly low catalytic activity in both catalytic processes.

ACKNOWLEDGMENTS

Financial support Project BG05M2OP001-1.002-0019 “Clean technologies for sustainable environment–water, waste, energy for circular economy” (Clean&Circle) is acknowledged. Dr. Nikolay Velinov for the Moessbauer spectra and Dr. Daniela Kovacheva for the XRD measurements is also acknowledged.

REFERENCES

1. "The Paris Agreement", UNFCCC, https://unfccc.int/process-and-meetings/the-paris-agreement/the-paris-agreement
2. "Net Zero by 2050 - A Roadmap for the Global Energy Sector", IEA, https://www.iea.org/reports/net-zero-by-2050
3. Szulejko J, Kwon E & Kim KH 2022, "Is mass-scale electrocatalysis of aqueous methanol an energetically and economically viable option for hydrogen production?", *J. Ind. Eng. Chem.* vol. 105, pp. 58–62.
4. Hakandai C, Pramono HS & Aziz M 2022, "Conversion of municipal solid waste to hydrogen and its storage to methanol", *Sust. Energy Technol. Assess*., vol. 51, p. 101968.
5. Ulejczyk B, Nogal L, Młotek M & Krawczyk K 2022, "Enhanced production of hydrogen from methanol using spark discharge generated in a small portable reactor*", Energy Reports,* vol. 8, pp.183–191.
6. Yu H, Li Y, Xu C, Jin F, Ye F & Li X 2022, "Distinct facets to enhance the process of hydrogen production via methanol steam reforming—A review*", Energy Stor. Sav.*, vol. 1, pp. 53–69.
7. Rana J, Sahoo S & Daw P 2021," Homogeneous first-row transition metal catalyst for sustainable hydrogen production and organic transformation from methanol, formic acid, and bio-alcohols" *Tetrahedron, v*ol. 99, p. 132473
8. "Convention on Long-Range Transboundary Air Pollution", United States Department of State, https://www.state.gov/key-topics-office-of-environmental-quality-and-transboundary-issues/convention-on-long-range-transboundary-air-pollution/
9. Guo Y, Wen M, Li G & An T 2021," Recent advances in VOC elimination by catalytic oxidation technology onto various nanoparticles catalysts: a critical review", *Appl. Catal. B: Environ.,* vol. 281, p. 119447.
10. Kamal MS, Razzak SA & Hossain MM 2016, "Catalytic oxidation of volatile organic compounds (VOCs): A review", *Atm. Environ*., vol. 140, pp. 117–134.
11. Yang C, Miao G, Pi Y, Xia Q, Wu J, Li Z & Xiao J 2019, "Abatement of various types of VOCs by adsorption/catalytic oxidation: A review", *Chem. Eng. J*., vol. 370, pp. 1128–1153.
12. Kharisov BI, Dias HV R & Kharissova OV 2019, „Mini-review: Ferrite nanoparticles in the catalysis", *Arabian J. Chem.*, vol. 12, pp. 1234–1246.
13. Mmelesi OK, Masunga N, Kuvarega A, Nkambule TT, Mamba BB & Kefeni KK 2021 "Cobalt ferrite nanoparticles and nanocomposites: Photocatalytic, antimicrobial activity and toxicity in water treatment", *Mater. Sci. Semicond. Process.*, vol. *123*, p. 105523.
14. Ceicilia ASJ, Dinesh A, Nirmala GF, Preetha AC, Slimani Y, Almessiere MA, Baykal A, Xavier B, Vinosha PA & Manikandan A 2021, **"**Review on recent advances of zinc substituted cobalt ferrite nanoparticles: Synthesis characterization and diverse applications", *Ceramics Inter.,* vol. 47, pp. 10512–10535.
15. Tatarchuk TR, Paliychuk ND, Bououdin M, Al-Najar B, Pacia M, Macyk W & Shyichuk A 2018**, "**Effect of cobalt substitution on structural, elastic, magnetic and optical properties of zinc ferrite nanoparticles", *J. Alloys Comp.*, vol. 731, pp. 1256–1266.
16. Narang SB & Pubby K 2021, "Nickel Spinel Ferrites: A review", *J. Magnet. Magnet. Mater*., vol. 519, pp. 167163.
17. Peng Y, Tang H, Yao B, Gao X, Yang X & Zhou Y 2021, "Activation of peroxymonosulfate (PMS) by spinel ferrite and their composites in degradation of organic pollutants: A Review", *Chem. Eng. J.,* vol. 414, p. 28800.

18. Hadjiivanov KI & Klissurski DG 1996, "Surface chemistry of titania (anatase) and titania supported catalysts" *Chem. Soc. Rev*., vol. 25, pp. 61–69.
19. Gong P, Xie J, Fang D, Liu XHF & Li F 2019, "Novel heterogeneous denitrification catalyst over a wide temperature range: Synergy between CeO_2, ZrO_2 and TiO_2", *Chem. Eng. J.,* vol. 356, pp. 598–608.
20. Chen HR, Shi JL, Yu J, Wang LZ & Yan DS 2000, "Synthesis of titanium-doped ordered porous zirconium oxide with high-surface-area", *Micropor. Mesopor. Mater*., vol. 39, pp. 171–176.
21. Sekuli J, Magraso A, Elshof JE & Blank DHA 2004, "Influence of ZrO_2 addition on microstructure and liquid permeability of mesoporous TiO_2 membranes", *Micropor. Mesopor. Mater.*, vol. 72, pp. 49–57.
22. Sun C, Zhu J, Lv Y, Qi L, Liu B, Gao F, Sun K, Dong L & Chen Y 2011, "Dispersion, reduction and catalytic performance of CuO supported on ZrO_2-doped TiO_2 for NO removal by CO", *Appl. Catal. B: Environ.*, vol. *103*, pp. 206–220.
23. Lyson-Sypien B, Czapla A, Lubecka M, Kusior E, Zakrzewska K, Radecka M, Kusior A, Balogh AG, Lauterbach S & Kleebe HJ 2013, "Gas sensing properties of TiO_2–SnO_2 nanomaterials", *Sens. Act. B* , vol. 187, pp. 445–454.
24. Yong Z, Linghu J, Xid S, Ru Tan H, Shen L, Yang P, Hui HK, Cao JQ, Leek ML, Yin X, Feng YP & Pan J 2018, "$Ti_{1-x}Sn_xO_2$ nanofilms: layer-by-layer deposition with extended Sn solubility and characterization", *Appl. Surf. Sci.,* vol. 428, pp. 710–717.
25. Liu Z, Guo B, Hong L & Jiang H 2005, "Preparation and characterization of cerium oxide doped TiO_2 nanoparticles", J. Phys. Chem. Solids, vol. 66, pp.161–167.
26. Tsoncheva T, Mileva A, Issa G, Dimitrov M, Kovacheva D, Henych J, Scotti N, Kormunda M, Atanasova G & Stengl V 2017, "Template-assisted hydrothermally obtained titania-ceria composites and their application as catalysts in ethyl acetate oxidation and methanol decomposition with a potential for sustainable environment protection", *Appl. Surf. Sci*., vol. 396, pp. 1289–1302.
27. Tsoncheva T, Mileva A, Issa G, Dimitrov M, Kovacheva D, Henych J, Kormunda M, Scotti N, Slušnác M, Tolasz J & Štengl V 2018, "Titania and zirconia binary oxides as catalysts for total oxidation of ethyl acetate and methanol decomposition", J. Environ. Chem. Eng., vol. 6, pp. 2540–2550.
28. Tsoncheva T, Issa G, Genova I, Dimitrova M, Kovacheva D, Henych J, Kormunda M, Scotti N, Tolasz J & Štengl V 2019, "Structure and catalytic activity of hydrothermally obtained titanium-tin binary oxides for sustainable environment: Evaluation and control", *Micropor. Mesopor. Mater.*, vol. 276, pp. 223–231.
29. Emeis CA 1993, "Determination of integrated molar extinction coefficients for infrared absorption bands of pyridine adsorbed on solid acid catalysts", *J. Catal*., vol. 141, pp. 347–354.
30. Pal J & Chauhan P 2009, "Structural and optical characterization of tin dioxide nanoparticles prepared by a surfactant mediated method", *Mater. Char.,* vol 60, pp. 1512–1516.
31. Arpac E, Sayılkan F, Asilturk M, Tatar P, Kiraz N & Sayılkan H 2007, "Photocatalytic performance of Sn-doped and undoped TiO_2 nanostructured thin films under UV and vis-lights", *J. Hazard Mater.,* vol.140, pp. 69–74.
32. Liqiang J, Honggang F, Baiqi W, Dejun W, Baifu X, Shudan L & Jiazhong S 2006, "Effects of Sn dopant on the photoinduced charge property and photocatalytic activity of TiO_2 nanoparticles" *Appl. Catal. B Environ.,* vol. 62, pp. 282–291.
33. Linnik O, Shestopal N, Smirnova N, Eremenko A, Korduban O, Kandyba V, Kryshchuk T, Socol G, Stefan N, Popescu-Pelin G, Ristoscu C & Mihailescu IN 2015, *"Correlation between electronic structure and photocatalytic properties of non-metal doped TiO_2/ZrO_2 thin films obtained by pulsed laser deposition method",* vol.114, pp. 166–171.

34. Bukauskas V, Kaciulis S, Mezzi A, Mironas A, Niaura G, Rudzikas M, Šimkienė I & Šetkus A 2015, "Effect of substrate temperature on the arrangement of ultra-thin TiO_2 films grown by a dc-magnetron sputtering deposition", *Thin Solid Films,* vol. 585, pp. 35-12.

35. Crist BV, *Handbook of Monochromatic XPS Spectra: The Elements of Native Oxides* 1999, XPS, International, LLC 754 Leona Lane, Mountain View, California 94040, USA.

36. Liu H, Wang M, Wang Y, Liang Y, Cao W & Su Y 2011, "Ionic liquid-templated synthesis of mesoporous CeO2–TiO2 nanoparticles and their enhanced photocatalytic activities under UV or visible light", *J. Photochem. Photobiol. A: Chem*., vol. 223, pp. 157–164.

37. Bhange PD, Awate SV, Gholap RS, Gokavi GS & Bhange DS 2016, "Influence of preparation methods on the structure and catalytic performance of SnO_2-doped TiO_2 photocatalysts", *Mater. Res. Bull.,* vol. 76, pp. 264–272.